Geochemical Perspectives Letters

Isotopic fractionation of neon during magma degassing

E. Núñez-Guerrero[1*], M. Moreira[1], B. Scaillet[1]

OPEN ACCESS

https://doi.org/10.7185/geochemlet.2505

Abstract

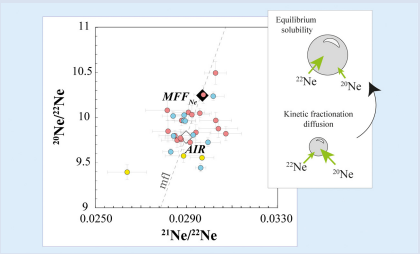

Determining the neon isotope composition of the Earth's mantle is key to unravelling how light noble gases became part of the primordial Earth. However, accurately measuring neon abundance and isotopic composition in primary mantle melts is challenging due to the low concentration of neon, coupled with potential isotopic fractionation during transport and degassing. Interestingly, natural samples that exhibit solar-like neon isotopic compositions, ranging between the values calculated for the Sun ($^{20}Ne/^{22}Ne = 13.36 \pm 0.09$; Heber *et al.*, 2012) and those resulting from solar wind implantation and sputtering ($^{20}Ne/^{22}Ne = 12.73$; Moreira and Charnoz, 2016), support the idea that the Earth's mantle might have trapped a primordial nebula in its early formation stages. Analyses of three synthetic vesiculated glasses, produced at ~1.7 kbar and 1200 °C using a starting material with an air-like isotopic composition ($^{20}Ne/^{22}Ne = 9.81$ and $^{21}Ne/^{22}Ne = 0.0287$) fluxed with CO_2, reveal significant isotopic fractionation of Ne within trapped vesicles. Measured values reach $^{20}Ne/^{22}Ne = 10.50 \pm 0.14$. The isotopic variations among individual vesicles align with expectations for kinetic fractionation, suggesting that degassing processes affect Ne isotope composition of basaltic melts.

Received 21 June 2024 | Accepted 13 January 2025 | Published 10 February 2025

Introduction

Determining the neon isotopic ratio of the Earth's mantle is fundamental to understanding the mechanism of incorporation of the noble gases in the primordial Earth. Two main models have been proposed to explain the origin of neon in the mantle: (i) solar nebula gas dissolution, and (ii) accretion of solar wind-irradiated material. The first model posits that neon was incorporated into a magma ocean after gravitational capture of a dense primary H_2-He atmosphere (Mizuno *et al.*, 1980; Harper Jr and Jacobsen, 1996; Yokochi and Marty, 2004; Mukhopadhyay, 2012; Williams and Mukhopadhyay, 2019). The second model proposes that neon was acquired before Earth's accretion on dust irradiated by the early Sun, in the inner solar system (Trieloff *et al.*, 2000; Ballentine *et al.*, 2005; Raquin and Moreira, 2009; Kurz *et al.*, 2009; Colin *et al.*, 2015; Moreira and Charnoz, 2016; Péron *et al.*, 2016, 2017, 2018). However, distinguishing between the solar nebula component and the implanted solar wind is challenging due to the similarity of their $^{20}Ne/^{22}Ne$ isotopic compositions; 13.36 ± 0.16 for the outer convective zone of the Sun and 12.52 – 12.75 for steady state composition of the solar wind (Black, 1972; Eberhardt *et al.*, 1972; Raquin and Moreira, 2009; Heber *et al.*, 2012; Moreira and Charnoz, 2016).

In terms of the isotopic composition of the light noble gases, particularly neon, the long term degassing process of the mantle results in differences in concentrations and isotopic compositions between Oceanic Island Basalts and Mid-Ocean Ridge basalts (OIBs and MORBs respectively). In the mantle, the production of ^{20}Ne and ^{22}Ne is negligible (Yatsevich and Honda, 1997), and thus the $^{20}Ne/^{22}Ne$ isotopic ratio can be considered to record the composition of primordial neon in the Earth's mantle. The lower mantle has undergone less degassing and retains higher concentrations of primordial noble gases, indicating the presence of an ancient, primordial composition. (Honda *et al.*, 1993; Moreira *et al.*, 1998; Ballentine *et al.*, 2005; Mukhopadhyay, 2012; Péron *et al.*, 2017; Trieloff *et al.*, 2000). Unlike MORB sources, plume sources exhibit different trends for the neon isotopic composition as seen, for instance, in the Galapagos plume, which is considered as one of the most primitive neon sources in terms of the nucleogenic neon isotopic composition ($^{21}Ne/^{22}Ne = 0.0345 \pm 0.0004$), with a $^{20}Ne/^{22}Ne$ isotopic ratio estimated to be 12.65 ± 0.04 (2σ) (Péron *et al.*, 2017). Values of $^{20}Ne/^{22}Ne$ higher than 12.65 are sometimes observed (*e.g.*, the South Atlantic, Iceland, and Kola Peninsula of Russia; Yokochi and Marty, 2004; Mukhopadhyay, 2012; Williams and Mukhopadhyay, 2019), which was interpreted as reflecting a mantle source having a neon composition similar to the solar nebula.

Step crushing is commonly used for the analysis of noble gases trapped in vesicles of basaltic glass during magma degassing (*e.g.*, Moreira *et al.*, 1998; Kurz *et al.*, 2009; Williams and Mukhopadhyay, 2019). The ensuing results yield mixing trends between atmospheric and mantle end members. Nonetheless, this method does not entirely remove the air component. The laser ablation technique pioneered by Burnard (1999) and Burnard *et al.* (1997) to analyse single bubbles, in combination with X-ray microtomography, allowed identifying vesicles connected to the surface by microfractures thereby avoiding analysing air contaminated bubbles (Raquin *et al.*, 2008; Péron *et al.*, 2016). Nevertheless, the possibility of isotopic fractionation during rapid vesiculation (*e.g.*, disequilibrium vesiculation; Aubaud *et al.*, 2004; Ruzié and Moreira, 2010) remains. The highest neon

1. ISTO, CNRS-Université d'Orléans-BRGM, 1a rue de la Férollerie, 45071, Orléans, France
* Corresponding author (email: elena.nunez@etu.univ-orleans.fr)

isotopic compositions measured by step crushing have typically been assumed to have minimal air contamination, providing a lower limit for the mantle (*e.g.*, Yokochi and Marty, 2004; Williams and Mukhopadhyay, 2019). However, the issue is compounded by the possible isotopic fractionation of neon during transport and degassing processes.

In basalt melts CO_2 is the main driver of volatile exsolution. Because CO_2 diffusion is slower than Ne (*e.g.*, Lux, 1987; Nowak *et al.*, 2004), early formed bubbles will get enriched in Ne. Additionally, it is assumed that lighter isotopes such as ^{20}Ne diffuse faster than heavier ones (^{22}Ne), a result of their contrasting molecular weights. This kinetic fractionation during disequilibrium degassing can elevate the $^{20}Ne/^{22}Ne$ ratios in the vesicles. However, this mechanism has not yet been experimentally tested.

This work aims, therefore, to provide such a test by analysing the neon isotopic composition of single vesicles in three experimental samples produced under controlled temperature and pressure conditions.

Materials and Methods

Since CO_2 forms the major gas in the vesicles of the submarine basalt samples from the Atlantic and Pacific (Moore *et al.*, 1977), and we are interested in the isotopic evolution of neon during magma nucleation and vesiculation, the main experimental variables for this study are the duration of the experiment and the amount of CO_2 introduced. Two types of experiments were conducted: (i) CO_2 only experiments, and (ii) CO_2 and Ne-bearing experiments. CO_2-rich experiments served to define the best conditions for producing bubble-rich glass (Fig. S-3), which was then used for the second type of experiments, the main focus of this study. The process of targeting vesicles (of only a few tens of microns; Fig. S-4b,c) amenable to laser ablation is indeed inherently time consuming, and it often requires days or weeks to locate a single vesicle.

For Ne-bearing experiments, the starting material was a basaltic glass previously doped in Ne, mixed with a Ne-free glass of the same composition in a wt. % ratio 1/10 (Supplementary Information and Table S-1). The Ne-doped glass was first prepared by melting the basaltic glass at 1400 °C under a continuous flow of pure Ne at 1 bar for 240 min; this glass was found to have a homogeneous distribution of air-like neon isotopic composition ($^{20}Ne/^{22}Ne = 9.81 \pm 0.01$ and $^{21}Ne/^{22}Ne = 0.0287 \pm 0.0001$; Tables S-2, S-3). The neon solubility of the glass was determined to be $3.16 \pm 0.38 \cdot 10^{-4}$ ccSTP $\cdot$ g^{-1} $\cdot$bar^{-1}.

CO_2 was introduced into the capsule in the form of solid $Ag_2C_2O_4$. During the experiment, the silver oxalate melted, releasing CO_2 as a gas. The amount of CO_2 used in each experiment varied (from 0.17 to 4.49 mg; 0.3–7.2 wt. %) being always enough to saturate the melt with CO_2 under the experimental P and T conditions. This approach enabled bubble nucleation and their upward transport within the capsule. Experiments were performed at pressures between 1535 and 2000 bars and 1200 °C, using sealed $Au_{80}Pd_{20}$ capsules, in an internally heated pressure vessel equipped with a drop quench system (see Supplementary Information for additional details). The duration of the experiments varied from 10 min up to 1800 min, the latter duration approaching equilibrium conditions with respect to CO_2 solubility (Pichavant *et al.*, 2018). Upon quenching, most recovered quenched glasses contained bubbles that were variably distributed across the samples. As shown below, in the longest run (1800 minutes), CO_2 solubility was achieved, and no vesicles were observed in the glass, having fully accumulated on the top of the capsules (sample *EN-E3*). Our procedure simulates the recharge of a degassed (*i.e.* CO_2 and neon-poor) shallow magmatic chamber under isothermal conditions by a melt rich in both CO_2 and neon.

The CO_2 content of quenched glasses was analysed by Fourier-Transform Infrared Spectroscopy (FTIR) (Table S-6). X-ray microtomography was used to characterise each experimental sample's vesicularity and localise the vesicles for laser ablation (Supplementary Information and Tables S-9, S-10 and Fig. S-3). The neon isotopic composition was analysed by coupling laser ablation and mass spectrometry (Table S-8).

Ne Fractionation during Vesiculation

A total of 26 experiments were conducted. Sixteen experiments, in which CO_2 was the sole volatile added, were aimed at examining the evolution of vesicularity over time. The largest average bubble diameter was 38 µm (*ESFa-5B-10min*), while the laser beam diameter was 35 µm, making bubble piercing challenging. Although microtomography helped identify bubble clusters in the samples, single bubble identification during the laser ablation process occurred mostly at random. Based on textural analyses, three out of ten experiments with neon and CO_2 were considered as the most promising and selected for subsequent analyses by mass spectrometry to explore neon isotopic fractionation.

Combining the textural data obtained by microtomography (vesicularity, mean diameter and the vesicle size distribution of each sample; Table S-9 and Fig. S-2) and the results from FTIR (Table S-6), a dynamic interplay is observed between bubble migration; B_d (which is influenced by the rate of bubble growth; G_r) and CO_2 diffusion within the melt; D_{CO2}. Figure 1 shows that during the first 240 min of our experiments, the D_{CO2}, and bubble growth, G_r, are more efficient than the vertical transport of bubbles, B_d, (Fig. 1). In contrast, after 240 min, the average bubble size is large enough for buoyancy to prevail over CO_2 diffusion.

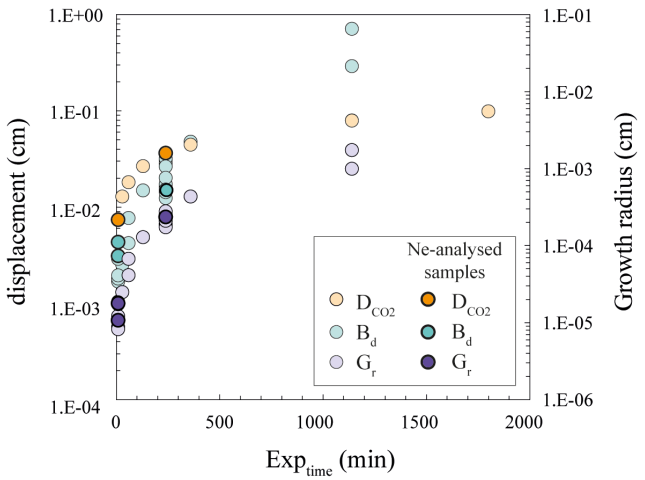

Figure 1 Comparison between CO_2 diffusion in the melt (D_{CO_2}; represented by orange dots) and the displacement of CO_2 bubbles toward the top of the capsule (B_d; represented by blue dots) which depends on bubble radius (G_r, purple dots). Each dot illustrates the state of these three parameters at the time the experiments were quenched. D_{CO2} and B_d are plotted on the left axis, while G_r is on the right, both using logarithmic scales for clarity. Intense colours highlight samples analysed for neon isotopic composition. Details on parameter calculations are provided in the Supplementary Information.

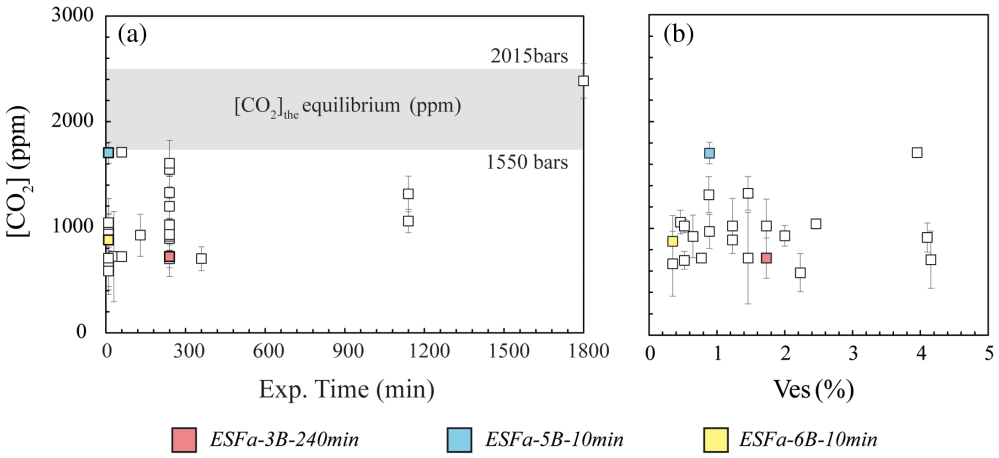

Figure 2 **(a)** Dissolved CO_2 over time and **(b)** comparison with the measured vesicularity of every experimental sample. The grey area points out the maximum CO_2 dissolved expected in the samples for the composition of the magma and the experiment conditions (1200 °C and 1.5–2 kbars; Jiménez-Mejías *et al.* (2021)). The samples analysed for neon isotope compositions are marked following the colour code used in the three neon isotope plot of Figure 3.

The results from FTIR analysis are plotted in Figure 2. The amount of CO_2 added to the experimental capsules had no effect on the dissolved CO_2 (Fig. 2a) or the final vesicularity (Fig. 2b) in samples quenched at the same experimental time. All samples, with the exception of *EN-E3*, plot outside equilibrium conditions (grey field), as shown by the heterogeneous CO_2 content of the glasses, which ranges from 585 up to 1710 ppm (Table S-6), varying by up to 50 % in different points of the same charge. In contrast, the glass of the 1800 min run (sample *EN-E3),* is vesicle-free and has a homogeneous CO_2 distribution of 2385 ± 162 ppm, which is the expected solubility value at the run conditions (equilibrium).

The three experimental samples selected for mass spectrometry are: samples *ESFa-5B* and *ESFa-6B,* corresponding to 10 min of experiment, and sample *ESFa-3B*, which was quenched at the time before the average distance travelled by the vesicles and the diffusion of CO_2 through the melt coincide in time, *i.e.* 240 min (Fig. 1 and Table S-10).

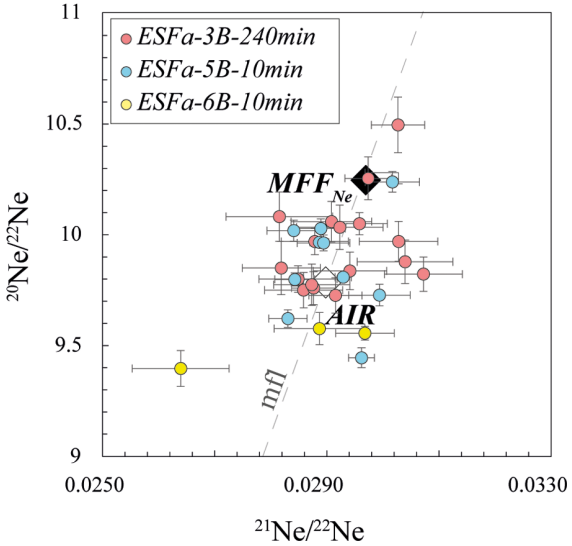

Figure 3 The three neon isotope plot for the vesicles. The black diamond represents the maximum theoretical fractionation factor, MFF_{Ne}, expected for the reference value ($^{20}Ne/^{22}Ne = 10.28$ and $^{21}Ne/^{22}Ne = 0.0297$); the white diamond represents the isotopic ratio of the Ne-bearing starting material ($^{20}Ne/^{22}Ne = 9.81$ and $^{21}Ne/^{22}Ne = 0.0287$). The dashed line represents the mass fractionation line, *mfl*. Data in Table S-8. Uncertainties are 1σ.

Given an air-like starting isotopic composition ($^{20}Ne/^{22}Ne = 9.8$ and $^{21}Ne/^{22}Ne = 0.0290$), the maximum fractionation factor, MFF_{Ne} for the neon isotopes can be estimated from Graham's law, which assumes that the isotopes of neon fractionate during diffusion, in accordance with their mass differences as:

$$MFF_{Ne} = r_{i/j} \cdot (m_j/m_i)^{1/2}$$

where $r_{i/j}$ is the air-like isotopic ratio, m is the mass, and i and j are the light and the heavy isotopes, respectively. This produces $^{20}Ne/^{22}Ne = 10.28$ and $^{21}Ne/^{22}Ne = 0.0297$.

The Ne isotopic compositions from twenty nine out of thirty one vesicles are shown in Figure 3. The plot does not include the vesicles *V2*, and *V9ALA* from sample *ESFa-3B-240min* for which a change of pressure measured during the expansion of the gas in the line after ablation shows that more than one vesicle was pierced (Fig. S-4). The dispersion of the measured Ne isotope ratios along the mass fractionation line suggests that isotopic fractionation occurred to some extent in the three experiments. The $^{20}Ne/^{22}Ne$ isotopic ratios reach values as high as the maximum fractionation factor expected for the initial composition; $V_{2ALA} = 10.50 \pm 0.13$ and $V_{3ALA} = 10.24 \pm 0.05$ for *ESFa-3B-240min* and V4 = 10.24 ± 0.05 for *ESFa-5B-10min* (Table S-8) within 1σ uncertainty. Some of the vesicles show neon isotopic ratios below the air-like starting composition (*e.g.,* V1 = 9.40 ± 0.08 for *ESFa-6B-10min*).

Discussion and Conclusion

This is the first experimental work on neon isotopic fractionation during degassing of a basaltic melt. Figure 4 shows a representative picture of the evolution of our experiments with time.

Figure 4a represents the material loaded in the capsule at time t = 0, before the release of CO_2 by the melting of $Ag_2C_2O_4$ and its subsequent transport through the grains of the basaltic powder. Figure 4b represents an early stage of bubble nucleation in the melt across the capsule. At the onset of the bubble nucleation, driven by CO_2, neon rapidly diffuses into the first nucleated bubbles. As stated previously, due to its higher

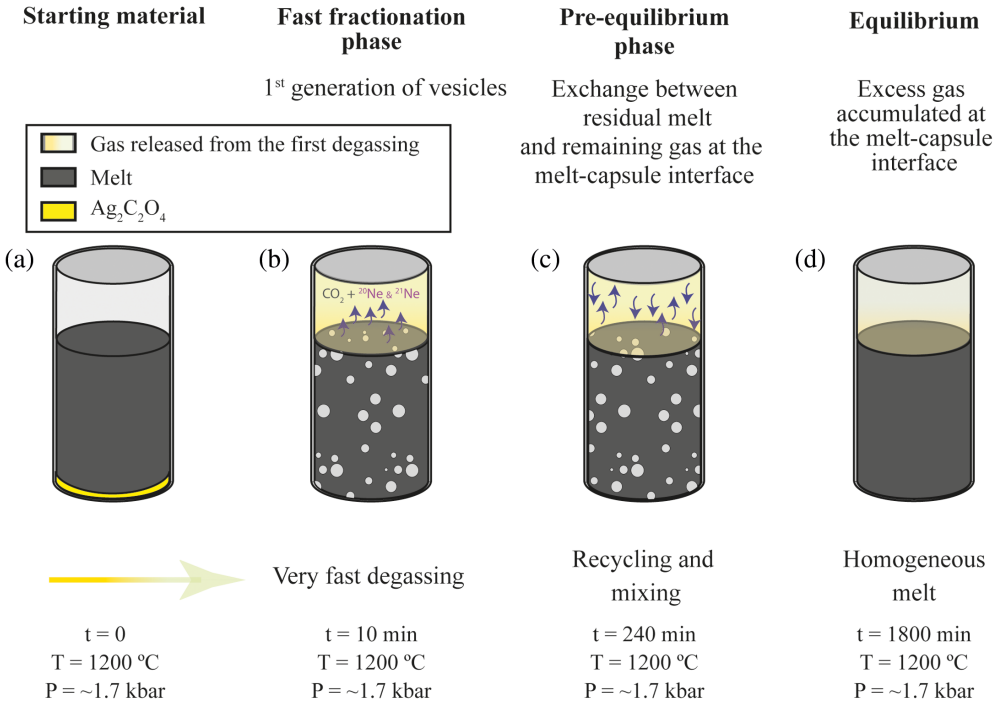

Figure 4 Representative evolution of our experiments from 10 to 1800 minutes. **(a)** The first capsule represents the start of the experiment, with the powdered starting material and the volatile component in the solid phase. The capsules in **(b)** and **(c)** show the experiments at 10 and 240 min. **(d)** shows the final stage of the melt and gas (1800 min, at equilibrium).

diffusivity, neon reaches the vesicles before the CO_2 reaches equilibrium between melt and gas (see Figs. 1, 4b). A significant quantity of gas accumulates at the interface between the melt and the capsule. The gas accumulated at the top of the capsule is presumably rich in ^{20}Ne and ^{21}Ne relative to ^{22}Ne. Correlatively, during this "*fast fractionation phase*" (Fig. 4b), the melt becomes depleted in these light isotopes. This explains the low $^{20}Ne/^{22}Ne$ and $^{21}Ne/^{22}Ne$ isotopic ratios (less than 9.66 and 0.0273 respectively, including the scatter error) observed in vesicles V_{10} and V_{11} in sample *ESFa-5B-10min* and the three analysed vesicles of sample *ESFa-6B-10min*. Unfortunately, the gas accumulated at the capsule-glass interface after quenching could not be analysed.

During the experiment, the gas trapped at the melt-capsule interface continuously interacts with the melt (Fig. 4c). Meanwhile, bubbles grow either through inward diffusion of CO_2 (since the pressure remains stable during the experiment, vesicles cannot grow by gas expansion) or through bubble coalescence and strive to reach isotopic equilibrium. This is the case for all of the analysed vesicles with air-like $^{20}Ne/^{22}Ne$ and $^{21}Ne/^{22}Ne$ isotopic ratios, mostly belonging to sample *ESFa-3B-240min* (Table S-8). However, newly formed bubbles (vesicles that continue to nucleate) are fractionated, and at this time, as the melt is interacting also with the gas accumulated at the capsule-melt interface (with high isotopic ratios as explained previously), and the resultant new vesicles have $^{20}Ne/^{22}Ne$ and $^{21}Ne/^{22}Ne$ isotopic ratios as high as 10.50 and 0.0303 respectively (vesicle V_2; Table S-8). Different generations of vesicles can be observed while the experiments last longer, with new nuclei of vesicles and vesicles with larger sizes compared to those formed in shorter experiments (Fig. S-2). As the duration of the experiments increases (from 10 to 1140 minutes), there is a noticeable decrease in the number of smaller vesicles (which correspond to the nuclei of new bubbles), an increase in the vesicle mean diameter, along with the accumulation of vesicles at the top capsule-melt interface, until the main body of melt is vesicle-free and the gas phase at the top of the capsule reaches equilibrium with the melt. The latter case is illustrated by the sample *EN-E3*, which lacks bubbles, and in which the measured dissolved CO_2 content is 2385 ± 162 ppm (Fig. 4d), in good agreement with the solubility determined by Jiménez-Mejías *et al.* (2021) (2487 ppm) for the conditions of the experiment, indicating attainment of equilibrium.

The results of our experiments demonstrate that in a system in which bubbles are continuously nucleating (*i.e.* while the system is oversaturated in CO_2) the last formed vesicles will tend to be kinetically fractionated until the diffusion of all isotopes of Ne reaches equilibrium. The same phenomenon can be expected to occur with other noble gases, as for example argon.

The principal implication of this work bears on the interpretation of the analyses of the gas trapped in magma vesicles in natural samples. Our findings suggest that when a CO_2-rich magma enters a reservoir, the resident magma might be unable to assimilate this new flux if degassing occurs too fast. This is due to the contrasted diffusivities of the various volatile species (here CO_2 and Ne) and of the different isotopes involved, producing a mass dependent isotope fractionation. Consequently, caution must be exercised when interpreting the highest values obtained from the analysis of noble gases in bubbles of natural samples (either by crushing extraction or by laser ablation of single vesicles), as faithfully recording the isotopic composition of the mantle source, in particular whenever fast degassing processes are suspected. While this work represents a critical step for identifying the source of neon in the Earth's mantle, for the time being it does not definitively favour any of the proposed scenarios. Yet, it shows that isotopic fractionation due to mass dependence could account for the high values observed in some natural samples, suggesting that the dissolution of the solar nebula in a magma ocean is not the only possible explanation.

Acknowledgements

The authors acknowledge support from LabEx VOLTAIRE (ANR-10LABX-100-01) and the European Research Council (ERC) (Grant agreement No.101096688[APATE][ERC-2022-ADG]). We are grateful to J. Andujar, I. Di Carlo, A. Slodczyk and P. Penhoud for their help during experiments and analyses as well as to the anonymous reviewers for their constructive comments.

Editor: Romain Tartèse

Additional Information

Supplementary Information accompanies this letter at https://www.geochemicalperspectivesletters.org/article2505.

Cite this letter as: Núñez-Guerrero, E., Moreira, M., Scaillet, B. (2025) Isotopic fractionation of neon during magma degassing. *Geochem. Persp. Let.* 34, 1–5. https://doi.org/10.7185/geochemlet.2505

References

Aubaud, C., Pineau, F., Jambon, A., Javoy, M. (2004) Kinetic disequilibrium of C, He, Ar and carbon isotopes during degassing of mid-ocean ridge basalts. *Earth Planetary Science Letters* 222, 391–406. https://doi.org/10.1016/j.epsl.2004.03.001

Ballentine, C.J., Marty, B., Sherwood Lollar, B., Cassidy, M. (2005) Neon isotopes constrain convection and volatile origin in the Earth's mantle. *Nature* 433, 33–38. https://doi.org/10.1038/nature03182

Black, D.C. (1972) On the origins of trapped helium, neon and argon isotopic variations in meteorites—II. Carbonaceous meteorites. *Geochimica Cosmochimica Acta* 36, 377–394. https://doi.org/10.1016/0016-7037(72)90029-4

Burnard, P. (1999) The bubble-by-bubble volatile evolution of two mid-ocean ridge basalts. *Earth Planetary Science Letters* 174, 199–211. https://doi.org/10.1016/S0012-821X(99)00254-X

Burnard, P., Graham, D., Turner, G. (1997) Vesicle-specific noble gas analyses of "popping rock": implications for primordial noble gases in Earth. *Science* 276, 568–571. https://doi.org/10.1126/science.276.5312.568

Colin, A., Moreira, M., Gautheron, C., Burnard, P. (2015) Constraints on the noble gas composition of the deep mantle by bubble-by-bubble analysis of a volcanic glass sample from Iceland. *Chemical Geology* 417, 173–183. https://doi.org/10.1016/j.chemgeo.2015.09.020

Eberhardt, P., Geiss, J., Graf, H., Grögler, N., Mendia, M., Mörgeli, M., Schwaller, H., Stettler, A., Krähenbühl, U., Von Gunten, H. (1972) Trapped solar wind noble gases in Apollo 12 lunar fines 12001 and Apollo 11 breccia 10046. *Proceedings of the Third Lunar Science Conference, Supplement 3, Geochemical et Cosmochemical Acta, The MIT press 2*, 1821–1856.

Harper Jr, C.L., Jacobsen, S.B. (1996) Noble gases and Earth's accretion. *Science* 273, 1814–1818. https://doi.org/10.1126/science.273.5283.1814

Heber, V.S., Baur, H., Bochsler, P., McKeegan, K.D., Neugebauer, M., Reisenfeld, D.B., Wieler, R., Wiens, R.C. (2012) Isotopic mass fractionation of solar wind: Evidence from fast and slow solar wind collected by the Genesis mission. *Astrophysics Journal* 759, 121. https://doi.org/10.1088/0004-637X/759/2/121

Honda, M., McDougall, I., Patterson, D.B., Doulgeris, A., Clague, D.A. (1993) Noble gases in submarine pillow basalt glasses from Loihi and Kilauea, Hawaii: a solar component in the Earth. *Geochimica Cosmochimica Acta* 57, 859–874. https://doi.org/10.1016/0016-7037(93)90174-U

Jiménez-Mejías, M., Andújar, J., Scaillet, B., Casillas, R. (2021) Experimental determination of H2O and CO2 solubilities of mafic alkaline magmas from Canary Islands. *Comptes Rendus Géoscience* 353, 289–314. https://doi.org/10.5802/crgeos.84

Kurz, M.D., Curtice, J., Fornari, D., Geist, D., Moreira, M. (2009) Primitive neon from the center of the Galápagos hotspot. *Earth Planetary Science Letters* 286, 23–34. https://doi.org/10.1016/j.epsl.2009.06.008

Lux, G. (1987) The behavior of noble gases in silicate liquids: Solution, diffusion, bubbles and surface effects, with applications to natural samples. *Geochimica. Cosmochimica Acta* 51, 1549–1560. https://doi.org/10.1016/0016-7037(87)90336-X

Mizuno, H., Nakazawa, K., Hayashi, C. (1980) Dissolution of the primordial rare gases into the molten Earth's material. *Earth Planetary Science Letters* 50, 202–210. https://doi.org/10.1016/0012-821X(80)90131-4

Moore, J.G., Batchelder, J.N., Cunningham, C.G. (1977) CO_2-filled vesicles in mid-ocean basalt. *Journal of Volcanology and Geothermal Research*, 2, 309–327. https://doi.org/10.1016/0377-0273(77)90018-X

Moreira, M., Kunz, J., Allegre, C. (1998) Rare gas systematics in popping rock: isotopic and elemental compositions in the upper mantle. *Science* 279, 1178–1181. https://doi.org/10.1126/science.279.5354.1178

Moreira, M., Charnoz, S. (2016) The origin of the neon isotopes in chondrites and on Earth. *Earth Planetary Science Letters* 433, 249–256. https://doi.org/10.1016/j.epsl.2015.11.002

Mukhopadhyay, S. (2012) Early differentiation and volatile accretion recorded in deep-mantle neon and xenon. *Nature* 486, 101–104. https://doi.org/10.1038/nature11141

Nowak, M., Schreen, D., Spickenbom, K. (2004) Argon and CO_2 on the race track in silicate melts: a tool for the development of a CO_2 speciation and diffusion model. *Geochimica Cosmochimica Acta* 68, 5127–5138. https://doi.org/10.1016/j.gca.2004.06.002

Péron, S., Moreira, M., Colin, A., Arbaret, L., Putlitz, B., Kurz, M.D. (2016) Neon isotopic composition of the mantle constrained by single vesicle analyses. *Earth Planetary Science Letters* 449, 145–154. https://doi.org/10.1016/j.epsl.2016.05.052

Péron, S., Moreira, M., Putlitz, B., Kurz, M. (2017) Solar wind implantation supplied light volatiles during the first stage of Earth accretion. *Geochemical Perspectives Letters* 3, 151–159. https://doi.org/10.7185/geochemlet.1718

Péron, S., Moreira, M., Agranier, A. (2018) Origin of light noble gases (He, Ne, and Ar) on Earth: A review. *Geochem. Geophysics Geosystems* 19, 979–996. https://doi.org/10.1002/2017GC007388

Pichavant, M., Le Gall, N., Scaillet, B. (2018) Gases as precursory signals: experimental simulations, new concepts and models of magma degassing. In: Gottsmann, J., Neuberg, J., Scheu, B. (Eds.) *Volcanic Unrest. From Science to Society*. Springer, 139–154. https://doi.org/10.1007/11157_2018_35.

Raquin, A., Moreira, M.A., Guillon, F. (2008) He, Ne and Ar systematics in single vesicles: mantle isotopic ratios and origin of the air component in basaltic glasses. *Earth Planetary Science Letters*. 274, 142–150. https://doi.org/10.1016/j.epsl.2008.07.007

Raquin, A., Moreira, M. (2009) Atmospheric $^{38}Ar/^{36}Ar$ in the mantle: implications for the nature of the terrestrial parent bodies. *Earth Planetary Science Letters* 287, 551–558. https://doi.org/10.1016/j.epsl.2009.09.003

Ruzié, L., Moreira, M. (2010) Magma degassing process during Plinian eruptions. *Journal of Volcanology and Geothermal Research* 192, 142–150. https://doi.org/10.1016/j.jvolgeores.2010.02.018

Trieloff, M., Kunz, J., Clague, D.A., Harrison, D., Allègre, C.J. (2000) The Nature of Pristine Noble Gases in Mantle Plumes. *Science* 288, 1036–1038. https://doi.org/10.1126/science.288.5468.1036

Williams, C.D., Mukhopadhyay, S. (2019) Capture of nebular gases during Earth's accretion is preserved in deep-mantle neon. *Nature* 565, 78–81. https://doi.org/10.1038/s41586-018-0771-1

Yatsevich, I., Honda, M. (1997) Production of nucleogenic neon in the Earth from natural radioactive decay. *Journal of Geophysical Research Solid Earth* 102, 10291–10298. https://doi.org/10.1029/97JB00395

Yokochi, R., Marty, B. (2004) A determination of the neon isotopic composition of the deep mantle. *Earth and Planetary Science Letters* 225, 77–88. https://doi.org/10.1016/j.epsl.2004.06.010

Geochemical Perspectives Letters

Isotopic fractionation of neon during magma degassing

E. Núñez-Guerrero, M. Moreira, B. Scaillet

Supplementary Information

The Supplementary Information includes:

- Material and Method
- Tables S-1 to S-10
- Figures S-1 to S-4
- Supplementary Information References

Material and Method

Experimental samples:

Starting material. The initial material comprises basanitic scoria from the northeastern vent of Fasnia volcano, which erupted in January 1975 in Tenerife, Spain. This composition has previously been used for CO_2 solubility experiments (Jiménez-Mejías *et al.*, 2021) which facilitated our experiments. The chemical major element composition of the glass is shown in Table S-1. The natural sample was first crushed and powdered by using an agate mortar and acetone to prevent friction and damage to the mortar. The powdered sample was then melted at 1400 °C and 1 bar for 240 min in a platinum crucible. At the end of the experiment, the crucible was rapidly removed from the furnace and dropped into water ensuring a fast quenching. After grinding the resulting glass, this sequence was repeated once to ensure a homogeneous, anhydrous and bubble/crystal-free glass which was used as a starting material in all experiments described below.

Major elements. All glasses produced in this study were mounted in epoxy resin, polished, and analysed using a Cameca SX-Five electron microprobe at the Orléans Earth Sciences Institute (ISTO), France. Analytical conditions included an accelerating voltage of 15 kV, a beam current of 10 nA, counting times of 10 seconds per element, and a defocused beam diameter of 20 µm to minimise alkali migration. The calibration of major elements was performed using the following standards: albite (Si, Na), $TiMnO_3$ (Mn, Ti), Al_2O_3 (Al), FeO (Fe), MgO (Mg), orthoclase (K), andradite (Ca), and apatite (P). PET analyser crystals were used for elements with lower-energy emissions (K, Ti, P, and Ca), while LiF analyser crystals were employed for higher-energy emissions (Fe and Mn) (Di Carlo *et a*l., 2006). The results are presented in Table S-1.

Ne-bearing glass. A portion of the starting material was used to produce the neon-bearing glass used for the experiments. We followed the same technique as Jambon *et al.* (1986). The starting glass powder was

equilibrated in a temperature-regulated electric furnace at 1400 ^{O}C, under a constant flux of neon at 1 bar of pressure for 270 min and quenched following the same procedure as with the starting material.

To evaluate the homogeneity of the starting glass, the ^{22}Ne concentration and the isotopic composition of four chunks of glass of about 0.1-0.2 mg each were first measured using a QMS700 quadrupole-type mass spectrometer hosted at the ISTO. The sample holder where the chunks of glass were charged was baked at 100 ^{O}C and pumped for at least one day to desorb any noble gases of the glass after quenching and the inner surfaces of the laser chamber, to avoid air contamination. Once the analytical blank was low enough to start the analysis (^{22}Ne less than $2.5 \cdot 10^{-13}$ cm^3), a laser-type Ytterbium-doped fibre was used to melt the glass and release its dissolved volatiles. Each analysed piece was heated for two min to verify its complete degassing. The gas was purified and measured in the mass spectrometer. The ^{22}Ne concentration and the ^{21}Ne/^{22}Ne isotopic composition are detailed in Table S-2. The measured solubility was $3.16 \pm 0.38 \cdot 10^{-4}$ cm^{3}STP $\cdot$ g^{-1} $\cdot$ bar^{-1}.

Additionally, two pieces of the same neon-bearing glass were analysed using the newly acquired Noblesse 5F-5M noble gas mass spectrometer at ISTO Orleans, France. This instrument can resolve most isobaric interferences, including the critical ^{40}Ar^{++} interference with ^{20}Ne^{+}, which is essential to this study. Importantly, the Noblesse 5F-5M was acquired after the analyses performed with the QMS700 and HELIX-SFT mass spectrometers discussed here. As such, its data serve as subsequent confirmation of the elemental and isotopic homogeneity of the neon in the starting material.

The neon-enriched glass contains neon at abundances too high for direct analysis with either the Noblesse 5F-5M or Helix-SFT mass spectrometers. To address this, the gas was expanded into a larger volume (1 l) prior to introduction into the purification line and a volume of 0.21 cm^3 was used to introduce only a small quantity of neon into the mass spectrometer. A schematic representation of the system is provided in Figure S-1. The gas extraction followed the same protocol as with the quadrupole. The same laser type as for the QMS700 was used to bring the glass into the liquid state for two minutes, releasing the gas until *manual valve a* (Figure S-1), which corresponds to a total volume of 1100 cm^3, from which an aliquot of 0.21 cm^3 was extracted for subsequent mass spectrometer analysis. The purification protocol closely follows the procedure outlined for the Helix-SFT in the laser ablation section because the line used for the Noblesse is the same as for the Helix-SFT. Upon entering the purification line, the gas undergoes an initial stage of purification using two titanium sponge getters as it expands. In the first stage, a hot titanium getter (operating at 700 °C) absorbs gas species such as CO_2, O_2, and N_2 for five minutes. After cooling to ambient temperature, this getter continues to trap H_2 for an additional ten minutes (Stout and Gibbons, 1955). The second titanium getter further refines the gas before it is sent to cryogenic traps. At this stage, noble gases—except for neon—are captured for 15 minutes using two Cryoscan CryoSorb cold-head traps. The first trap, filled with stainless steel, adsorbs heavier noble gases (Ar, Kr, and Xe), while the second trap, made of activated charcoal, traps helium and neon and can be used to separate He from Ne. The results, summarised in Table S-3, include the ^{20}Ne/^{22}Ne and ^{21}Ne/^{22}Ne isotopic ratios derived from multiple gas aliquots (5 to 10): Table S-4 presents the run standards used throughout the analysis period. This procedure effectively minimised the blank contribution, which in this case was less than 21 %.

Capsule preparation and experimental set-up. Each capsule is set up from an $Au_{80}Pd_{20}$ tube of 2.9 mm outer diameter, 0.4 mm wall thickness and 1.5 cm length. A representative drawing of the experimental capsule is shown in Figure 4. The capsule was loaded with (1) Ne-free powdered basaltic glass, (2) silver oxalate as a source of CO_2, and (3) Ne-bearing basaltic glass for those experiments carried out with Ne. The mass of each component is given in Table S-5. The experiments were run in Internally Heated Pressure Vessels (IHPV) at ISTO, France. The experimental conditions are shown in Table S-5. All experiments were terminated by drop-

quenching (Di Carlo *et al*., 2006). A single experiment typically involved running two or more capsules simultaneously. This approach enabled us to test the same experimental conditions (P-T-duration) with varying amounts of CO_2 so as to observe its impact on vesicularity.

X-ray microtomography acquisitions

X-ray computed tomography is a non-destructive technique that allows for the precise localisation of vesicles prior to their puncturing, enabling the analysis of the gas by mass spectrometry and the characterisation of the vesicle size distribution (VSD) of the quenched glasses. The data were collected at ISTO with a Nanotom Phoenix micro-tomography system, which is equipped with a 180 kV X-ray tube with variable filament currents (40 - 170 µA) and an operating voltage of up to 120 kV.

The biggest piece of glass of every experimental capsule (sometimes several pieces at the same time) was mounted on a carbon fibre rod with a thermoplastic adhesive and then placed into the instrument to be rotated 360^{O} for the scan. Between 700 and 2000 projections were acquired with a resolution of 3 to 3.5 µm per pixel. The reconstruction of the acquired images in stacks was made via 3D with VGSudioMax. The first step is to correct for artefacts using a median filter and separating different density bands. Then we separated the portion of glass from the vesicles and the air surrounding the glass.

The microtomography images were processed using *ImageJ* to obtain the different VSDs in 2D. The *"analyse particles*" plugin was used after adjusting the threshold to obtain the surface of the glass and vesicles independently in each slice of the 2D image stack.

Vesicularity. The vesicularity of the samples was calculated using *VGStudioMax* by separating the volume of the glass from the volume occupied by the vesicles. Vesicularity is shown in Table S-9. Figure S-2 illustrates the evolution of vesicularity over time, with a representative example for each of the experiments.

Fourier-transform infrared spectroscopy (FTIR):

One or two chunks of glass for every quenched glass were doubly-polished for infrared spectroscopy analyses to thicknesses of 25-107 µm. The FTIR spectra were collected in transmission using a Nicolet 6700 FTIR spectrometer attached to an IR microscope (Nicolet Continuum) equipped with an MCT-detector at ISTO. CO_2 and H_2O contents were determined using a LEITZ DMR optical microscope equipped with an electronic X-Y stage. The absorbances of carbonate bands (≈1430 and ≈1525 cm^{-1}) and OH stretching vibration (≈3525 cm^{-1}) were determined by performing a first subtraction with the spectrum of an anhydrous decarbonated sample (the starting material in the mid-infrared (MIR) region, scaled to the same thickness, and then drawing a linear baseline below the H_2O bending and carbonate vibration bands). Typically, 128-256 scans were collected for each spectrum in the range of 1000 to 4000 cm^{-1}, with a window aperture of 40 x 40 and 20 x 20 µm and a spectral resolution of 4 cm^{-1}, collecting background on NaCl windows before each sample. The H_2O and CO_2 concentrations in the experimental glasses were determined using the Beer-Lambert law (*e.g.*, Stolper, 1982):

$$C_i = 100 \times (M_i \times A_j)/(d \times \rho \times \varepsilon_j)$$

Where C_i is the concentration of the species i in wt.%, M_i is the molecular weight of the species, A_j is the absorbance (peak height), d is the thickness of the section at each analysed point, ρ is the density of the sample (in $g \cdot l^{-1}$) and $\mathcal{E}_j$ is the absorption coefficient of band j (in $l \cdot mol^{-1} \cdot cm^{-1}$).

Despite that no water was added to the capsules, some FTIR spectra show a small amount of dissolved water generated through the reduction of Fe^{3+} of the melt during the synthesis. Thus, we decided to use the carbonate

peak of 1430 cm^{-1}, since the 1525 cm^{-1} band is slightly affected by the H_2O bending at 1630 cm^{-1}, to calculate the amount of CO_2 dissolved into the glass. Hence, the absorption coefficient considered for the 1430 cm^{-1} peak is 283 ± 8 l · mol^{-1} · cm^{-1}. The results for CO_2 and water contents are shown in Table S-6.

Laser ablation analyses:
The experimental samples were loaded into the laser cell under vacuum and baked at 100 ºC until the blank in the line was low enough ($^{22}Ne \approx 3 \cdot 10^{-13}$ cm^3STP) to start with the analysis. The drilling was done with a diode-pumped air-cooled Q-switched laser of 263 nm wavelength and 35 µm diameter, which works by repetition of power plasma pulses. This tool allows us to drill by ablation our glass chunks which are mm thick (Figure S-3) and be very precise in reaching micrometric bubbles. The pressure in the laser cell was continuously measured (in millibars) with a manometer MKS Baratron® 1 Torr full scale. When the laser ablation starts, a smooth increase in pressure happens (corresponding to the ablation of the glass). When a bubble is reached, a sharp change in the pressure is observed (Fig. S-5), and the ablation is stopped. Gas purification then starts, as explained next.

Once the gas is released from a pierced bubble the first stage of purification is performed with two Ti-sponge getters while the volume of the gas expands into the line. As explained above, during five minutes, the first hot Ti-getter (800 ºC) adsorbs chemical species like CO_2, O_2, and N_2 and then, at ambient temperature after cooling, trap H_2 for ten minutes (Stout and Gibbons, 1955). A second Ti-getter repeats the process. The noble gases, except Ne, were adsorbed for 15 minutes on activated charcoal in two cold fingers at liquid N_2 temperature. One cold finger is positioned at the end of the purification line, trapping 99 % of Ar. An additional cold finger is placed at the entrance of the mass spectrometer to reduce Ar^{++} interference before and during the Ne analysis. Before introducing Ne into a Helix-Split Flight Tube (ThermoFisher) mass spectrometer, we measured two cycles of Ne isotopes to stabilize the magnet. ^{20}Ne was measured using a mass scan instead of setting the magnet on the required field to measure ^{20}Ne, using an acceleration voltage of 4.5 kV and a trap current of 250 µA for the secondary electron multiplier (SEM) configuration.

Then Ne is introduced into the mass spectrometer. In addition to masses 20, 21, and 22, we also measured masses 40 and 44 for correcting isobaric interferences between Ar^{++} and $^{20}Ne^{+}$ and CO_2^{++} and ^{22}Ne. Fifteen cycles of measurement were done for every single vesicle, blank or standard. The acquisition software and the data processing were homemade using C# and MATLAB© respectively. The static background in the mass spectrometer was checked and estimated regularly ($^{20}Ne = 14.26 \cdot 10^{-12}$ and $^{22}Ne = 1.19 \cdot 10^{-13}$ cm^3STP). We determined the ionisation ratios $Ar^{++}/Ar^{+} = 0.03$ and $CO_2^{++}/CO_2^{+} = 0.0015$ for the Helix-SFT and corrected the partial contribution by introducing the parameters in the data processing code. The mass discrimination of the mass spectrometer is determined by averaging the standards measured over the course of the analysis of the vesicles. The standard used comes from the dilution of a volume of "one pipette" (0.1 cm^3) of atmospheric air in a reservoir of 2 l. The uncertainty in the mass discrimination is represented by the standard deviation of these standards (Table S-7). The Ne blank contribution was between 3 and 20 % except for V_7 in sample *ESFa-3B-240min* for which it was 30 %. After ablating the matrix for 10 min the matrix blank contributed to 70 %. Therefore, the correction was done directly using the line blank, since the matrix contribution can be considered negligible. Uncertainties on the isotopic ratios in the samples are derived from the propagation of the measured uncertainty, the blank correction, and the mass discrimination correction. The results of the vesicle analyses are shown in Table S-8.

Calculations:
Maximum mass fractionation factor (MFF_{Ne}). The maximum fractionation factor, was calculated using Graham's law, resulting in values of $^{20}Ne/^{22}Ne = 10.28$ and $^{21}Ne/^{22}Ne = 0.0297$. These were determined as $^{20}Ne/^{22}Ne_{Air} \cdot (m_{22}/m_{20})^{1/2}$ and $^{21}Ne/^{22}Ne_{Air} \cdot (m_{22}/m_{21})^{1/2}$ respectively.

To study the relationship between CO_2 diffusion in the melt, the displacement of bubbles along the capsule and the average growth of vesicles in the magma before quenching (Fig. 1), we calculate the following parameters.

Bubble radius growth (G_r). The growth rate of the bubbles, G_0, can provide useful information about the experimental samples. This parameter is independent of bubble size and gives information about the residence time of the bubbles in the magma, τ. Watson *et al.* (1982) calculated this value for basaltic melts using the diffusivity laws for dissolved CO_2, but Sarda and Graham (1990) observed that this value is significantly influenced by the initial CO_2 content of the magma, which is currently unknown. Consequently, the value of G_0 can vary by several orders of magnitude. In our experiments, the initial CO_2 content is known. The formula of τ, was deconvolved in order to calculate *Gr* in our experimental samples, and τ was fixed at 1800 minutes which is the time at which the run product glasses showed no more vesicles (sample *EN-E3*).

$$G_r = [1 / (\tau \times (-a))] \times time_{exp}$$

Where a is the slope of the vesicle size distribution (VSD) trend of each sample in cm and $time_{exp}$ is the time that the experiments run. These parameters, obtained by the 2D-image scan analyses are reported in Table S-9).

CO_2 diffusion in the melt (D_{CO2}). The predominant C-bearing species in basaltic melts is CO_3^{2-} (Zhang *et al.*, 2007). Because of the similarity in atomic size and mass to Ar, CO_2 diffusion is approximately the same as the chemical diffusivity of Ar in silicate melts (Zhang and Xu, 1995; Behrens and Zhang, 2001; Nowak *et al.*, 2004; Zhang *et al.*, 2007), and is described as:

$$Ln\, D_{melt} = -13.99 - (17367 + 1.9448 \times P) / T + [(855.2 + 0.2712 \times P) \times Cw] / T$$

$$D_{CO2} = D_{melt} \times time_{exp}$$

Where D_{melt} is CO_2 diffusivity in $m^2\ s^{-1}$, P is the pressure in MPa, T is the temperature in Kelvins, and Cw is the weight per cent of H_2O.

Bubble displacement (B_d). The bubble ascent rate, v_b was calculated using Stokes' Law, which describes the motion of a spherical particle through a viscous fluid.

$$v_b = -2/9 \times \left(r^2 \times g \times (\rho_b - \rho_L)\right) / \eta$$

Where r is the mean radius of the vesicles in meters, g is the gravity in $m \cdot s^{-1}$, ρ_b and ρ_L are the densities of the bubble (from Bottinga and Richet (1981) for the conditions of the experiment and the liquid respectively in $kg \cdot m^{-3}$, and η is the viscosity of the magma in $Pa \cdot s^{-1}$, calculated for each experiment using the amount of dissolved water and the experimental pressure, following the method of Giordano *et al.* (2008). The average distance of bubbles displacement during each experiment is given by:

$$B_d = v_b \times time_{exp}$$

The results are shown in Table S-10 and plotted in Figure 1. The parameters needed for the calculations can be found in Tables S-6 and S-9. In addition, the evolution of vesicularity in 3D over time is shown in Figure S-2.

Supplementary Tables

Table S-1 To ensure consistency with the data of the natural sample published by Jiménez-Mejías *et al.* (2021) (Basanite FAS*) the composition of the starting glass and the Ne-bearing glass were normalized to 100 % anhydrous (**). The sum of oxides (original totals ***) was as high as 99 %. All Fe is reported as FeO, and the standard deviation. Oxide concentrations (wt. %) measured by electron microprobe analysis at Orléans Earth Sciences Institute, France (ISTO).

	Basanite FAS*	Starting mat. **	Ne-bearing glass**	Starting mat. ***	Ne-bearing glass***
SiO_2	45.08 ± 0.14	44.86 ± 0.23	45.47 ± 0.15	44.27 ± 0.33	44.95 ± 0.28
TiO_2	3.82 ± 0.13	3.70 ± 0.18	3.78 ± 0.14	3.65 ± 0.16	3.74 ± 0.14
Al_2O_3	14.45 ± 0.17	14.87 ± 0.17	14.94 ± 0.17	14.67 ± 0.17	14.77 ± 0.12
FeO*	12.51 ± 0.27	12.39 ± 0.24	11.49 ± 0.43	12.22 ± 0.26	11.36 ± 0.48
MnO	0.28 ± 0.05	0.17 ± 0.07	0.11 ± 0.06	0.17 ± 0.07	0.11 ± 0.06
MgO	7.15 ± 0.22	7.80 ± 0.05	7.8 ± 0.11	7.69 ± 0.04	7.71 ± 0.10
CaO	10.82 ± 0.17	10.38 ± 0.10	10.43 ± 0.16	10.24 ± 0.12	10.31 ± 0.11
Na_2O	3.6 ± 0.10	3.63 ± 0.07	3.77 ± 0.08	3.59 ± 0.08	3.73 ± 0.06
K_2O	1.57 ± 0.07	1.47 ± 0.15	1.49 ± 0.04	1.45 ± 0.15	1.47 ± 0.05
P_2O_5	0.71 ± 0.07	0.73 ± 0.09	0.71 ± 0.05	0.72 ± 0.08	0.71 ± 0.05
$Na_2O + K_2O$	5.17	5.10	5.26	5.03	5.20
Total	100	100	100	98.67	98.85

Table S-2 ^{22}Ne abundances (in cm^3 STP/g) and $^{21}Ne/^{22}Ne$ ratio obtained with the quadrupole mass spectrometer for the Ne-bearing glass chunks analysed for checking homogeneity. The glass was free of vesicles and melted for 2 min under vacuum. The error associated with the abundance and the isotopic values is calculated as 1σ. The error associated with the average is obtained by the standard deviation of the four values.

Sample	mass $\cdot 10^{-4}$ g	$^{22}Ne \cdot 10^{-9}$ cm^3 STP / g	$^{21}Ne/^{22}Ne$	Solubility $\cdot 10^{-4}$ cm^3 STP / g · bar
Test6-s1	2.32	9.67 ± 0.04	0.0296 ± 0.0015	3.26
Test6-s2	1.24	10.79 ± 0.04	0.0285 ± 0.0014	3.63
Test6-s3	2.04	8.86 ± 0.02	0.0299 ± 0.0015	2.98
Test6-s4	1.40	8.19 ± 0.02	0.0295 ± 0.0015	2.76
Average		**9.38 ± 1.12**	**0.0294 ± 0.0006**	**3.16 ± 0.38**

Table S-3 ^{22}Ne abundances (in cm^3 STP/g) and ^{20}Ne/^{22}Ne and ^{21}Ne/^{22}Ne ratios measured with the Noblesse 5F-5M mass spectrometer for two neon-bearing glass samples (Test7-s1 and Test7-s2), analysed to check their isotopic composition and homogeneity. The # symbol denotes repeated measurements to test reproducibility, with each measurement corresponding to a new set of aliquots (see Vol 2 in Figure S-1). The glass, free of vesicles, was brought back to liquid state under vacuum for 2 minutes. The error associated with the abundance and the isotopic values is calculated as 1σ. The error associated with the average is obtained by the standard deviation of the test values.

Sample	mass · 10^{-4} g	Number of Aliquots	Blank	measured ^{22}Ne · 10^{-8} cm^3 STP / g	^{20}Ne/^{22}Ne	^{21}Ne/^{22}Ne
Test7-s1 #1	1.18	5	21.07 %	1.22	9.87 ± 0.07	0.0287 ± 0.0010
Test7-s1 #2	1.18	10	14.46 %	1.84	9.78 ± 0.05	0.0290 ± 0.0008
Test7-s1 #3	1.18	10	14.71 %	1.81	9.87 ± 0.05	0.0291 ± 0.0009
				Average	**9.84 ± 0.05**	**0.0289 ± 0.0002**
Test7-s2 #1	2.30	10	5.81 %	2.59	9.82 ± 0.03	0.0288 ± 0.0005
Test7-s2 #2	2.30	10	5.84 %	2.58	9.80 ± 0.03	0.0287 ± 0.0005
				Average	**9.81 ± 0.01**	**0.0287 ± 0.0001**

Table S-4 Measured neon isotopic ratios (corrected for blanks) of the Ne-standard (for the Noblesse 5F-5M mass spectrometer). This set was analysed over ten days, the averages for the two isotopic ratios are represented with the associated 1sigma uncertainties. To correct for mass discrimination, averages of isotopic ratios measured on standards during the same period as for ne-bearing glass were taken as well as an average of 7.02 $\cdot 10^{-15}$ cm^3 STP $\cdot$ cps^{-1} for the sensitivity of ^{22}Ne. The uncertainty of the average represents the standard deviation of the reported set standards.

		Sensitivity $^{22}Ne \cdot 10^{-15}$ (cm^3STP / cps)	**$^{20}Ne/^{22}Ne$**	**$^{21}Ne/^{22}Ne$**
Day 1	STD_1	6.99	10.05 ± 0.02	0.0288 ± 0.0004
	STD_2	7.01	10.04 ± 0.02	0.0300 ± 0.0004
	STD_3	7.03	10.05 ± 0.02	0.0293 ± 0.0003
	STD_4	7.03	10.04 ± 0.02	0.0298 ± 0.0003
	STD_5	7.01	10.03 ± 0.02	0.0300 ± 0.0004
	Average		**10.04 ± 0.01**	**0.0296 ± 0.0005**
Day 2	STD_6	6.96	10.00 ± 0.02	0.0295 ± 0.0003
	STD_7	6.96	10.02 ± 0.02	0.0292 ± 0.0004
	STD_8	6.92	10.00 ± 0.02	0.0298 ± 0.0003
	STD_9	6.88	9.97 ± 0.02	0.0298 ± 0.0003
	STD_10	6.92	10.05 ± 0.02	0.0289 ± 0.0003
	STD_11	6.92	10.05 ± 0.02	0.0295 ± 0.0003
	Average		**10.01 ± 0.03**	**0.0294 ± 0.0003**
Day 3	STD_12	7.20	10.04 ± 0.02	0.0292 ± 0.0004
	STD_13	7.12	10.00 ± 0.02	0.0297 ± 0.0004
	STD_14	7.13	10.05 ± 0.02	0.0294 ± 0.0003
	STD_15	7.11	10.05 ± 0.02	0.0298 ± 0.0004
	STD_16	7.10	10.09 ± 0.02	0.0300 ± 0.0004
	STD_17	7.08	10.04 ± 0.02	0.0294 ± 0.0003
	STD_18	7.00	10.04 ± 0.02	0.0296 ± 0.0004
	mean		**10.04 ± 0.02**	**0.0296 ± 0.0003**
Day 4	STD_19	7.05	10.0 ± 0.02	0.0292 ± 0.0004
	STD_20	7.04	10.03 ± 0.02	0.0298 ± 0.0004
	STD_21	7.03	10.03 ± 0.02	0.0296 ± 0.0003
	STD_22	7.05	10.06 ± 0.02	0.0294 ± 0.0003
	mean		**10.04 ± 0.01**	**0.0295 ± 0.0003**
Day 5	STD_23	6.90	10.04 ± 0.02	0.0294 ± 0.0003
	STD_24	6.96	10.15 ± 0.02	0.0295 ± 0.0003
	STD_25	6.98	10.14 ± 0.02	0.0297 ± 0.0003
	STD_26	7.02	10.14 ± 0.02	0.0296 ± 0.0004
	STD_27	7.06	10.14 ± 0.02	0.0289 ± 0.0004
	STD_28	7.08	10.13 ± 0.02	0.0298 ± 0.0003
	mean		**10.12 ± 0.04**	**0.0295 ± 0.0003**

Table S-5 Experimental conditions. # indicates the experimental run; CO_2, Ne-bearing glass and powder of starting material loaded into the capsule in mg. *P* and *T* are the conditions in the IHPV. $time_{exp}$ is the time at which the experiment was quenched.

Sample	Run	Starting mat. $\cdot 10^{-3}$ g	CO_2 added $\cdot 10^{-3}$ g	Ne-bearing glass $\cdot 10^{-3}$ g	T °C	P_{exp} bar	$time_{exp}$ min
CO_2-bearing glass samples							
ESFa-4	#2	63.20	0.75	-	1200	1598	30
ESFa-8	#3	60.10	0.84	-	1200	1609	240
ESFa-10	#3	58.10	4.49	-	1200	1609	240
ESFa-10E	#7	62.00	0.87	-	1200	1726	1140
ESFa-2D	#7	62.30	3.59	-	1200	1726	1140
ESFa-3D	#8 + 9	55.20	0.38	-	1200	1725	130
ESFa-8D	#10 +11	63.70	2.96	-	1200	1674	360
ESFa-1C	#12	58.90	1.56	-	1200	1671	10
ESFa-2C	#12	56.50	3.10	-	1200	1671	10
ESFa-4C	#13	61.80	0.93	-	1200	1683	60
ESFa-5C	#13	61.80	3.56	-	1200	1683	60
ESFa-6C	#15	58.60	0.41	-	1200	1605	240
ESFa-7C	#15	61.30	4.00	-	1200	1605	240
ESFa-9C	#14	78.20	3.42	-	1200	1660	10
ESFa-10C	#15	61.80	0.81	-	1200	1605	240
ESFa-1B	#14	64.60	0.87	-	1200	1660	10
CO_2+Ne-bearing glass samples							
ESFa-1B	#1	60.70	1.83	6.60	1200	1535	240
ESFa-2B	#1	63.80	0.84	6.50	1200	1535	240
ESFa-3B	#1	51.60	0.84	5.40	1200	1535	240
ESFa-5B	#2	60.40	1.80	6.00	1200	1573	10
ESFa-6B	#2	63.50	3.74	6.30	1200	1573	10
ESFa-7B	#4	63.50	0.90	6.50	1200	1605	240
ESFa-10B	#4	64.10	3.83	6.30	1200	1605	240
ESFa-2A	#4	59.90	0.96	6.30	1200	1605	240
ESFa-5A	#5	62.50	3.65	6.60	1200	1669	10
EN-E3	#7	57.90	0.17	5.90	1200	2015	1800

Table S-6 FTIR data. The average of H_2O and CO_2 concentration was calculated from the number of analytical spots in each sample, the results shown below were calculated using the error propagator developed by the « Digital modelling platform» of ISTO. The thickness belongs to the spot where the analysis was done. Thickness was measured five times at every analysed spot, and the thickness uncertainty corresponds to the standard deviation of these measurements. The density of the silicate liquid, δ_l, was determined using the model of Lange (1994) and Warren (1995). A_{1430} and A_{3525} are the absorbance of the fundamental OH-stretching vibration (~3525 cm^{-1}) and the carbonate doublet (~1430 cm^{-1}) in the mid-infrared (MIR) region.

Sample	Thickness · 10^{-3} cm	δ_L g · l^{-1}	A_{1430}	*sd*	A_{3525}	*sd*	[CO_2] ppm	H_2O wt. %
CO_2-bearing glass								
ESFa-4.3	3.32 ± 0.36	2722 ± 15	0.060	0.002	-	-	722 ± 429	
ESFa-4.4	5.10 ± 0.40	2722 ± 15	0.037	0.003	-	-		
ESFa-8.1	5.58 ± 0.13	2717 ± 7	0.087	0.005	0.063	0.002	893	0.13
ESFa-10.1	4.98 ± 0.18	2734 ± 41	0.114	0.004	0.064	0.003	1022 ± 252	0.10 ± 0.03
ESFa-10.2	6.20 ± 0.21	2734 ± 41	0.088	0.003	0.044	0.002		
ESFa-10.3	5.58 ± 0.13	2734 ± 41	0.095	0.005	0.044	0.003		
ESFa-10E.1	6.06 ± 0.24	2739 ± 4	0.121	0.007	0.239	0.003	1315 ± 169	0.47 ± 0.04
ESFa-10E.4	4.94 ± 0.36	2739 ± 4	0.117	0.004	0.231	0.001		
ESFa-10E.5	4.90 ± 0.25	2739 ± 4	0.136	0.002	0.217	0.002		
ESFa-10E.6	5.52 ± 0.20	2739 ± 4	0.118	0.006	0.217	0.001		
ESFa-2D.1	8.46 ± 0.19	2751 ± 7	0.162	0.006	0.303	0.002	1059 ± 111	0.39 ± 0.04
ESFa-2D.2	8.68 ± 3.40	2751 ± 7	0.144	0.007	0.274	0.002		
ESFa-2D.3	8.58 ± 0.31	2751 ± 7	0.175	0.004	0.336	0.002		
ESFa-3D.1	3.04 ± 0.67	2772 ± 44	0.063	0.002	-	-	925 ± 200	
ESFa-3D.2	5.92 ± 0.47	2772 ± 44	0.085	0.002	-	-		
ESFa-3D.3	5.92 ± 0.47	2772 ± 44	0.086	0.002	-	-		
ESFa-8D.1	9.68 ± 0.11	2735 ± 13	0.111	0.005	-	-	702 ± 114	
ESFa-8D.3	9.16 ± 0.17	2735 ± 13	0.113	0.004	-	-		
ESFa-8D.4	9.40 ± 0.16	2735 ± 13	0.126	0.009	-	-		
ESFa-8D.4.2	9.66 ± 0.11	2735 ± 13	0.117	0.004	-	-		

Sample	Thickness · 10^{-3} cm	δ_L g · l^{-1}	A_{1430}	*sd*	A_{3525}	*sd*	[CO_2] ppm	H_2O wt. %
ESFa-8D.5	10.66 ± 0.38	2735 ± 13	0.164	0.005	-	-		
ESFa-8D.6	9.64 ± 0.18	2735 ± 13	0.090	0.002	-	-		
ESFa-1C.1	5.50 ± 0.24	2762 ± 56	0.086	0.002	-	-	971 ± 159	
ESFa-1C.2	5.36 ± 0.13	2762 ± 56	0.084	0.003	-	-		
ESFa-1C.3	6.68 ± 0.41	2762 ± 56	0.137	0.004	-	-		
ESFa-2C.1	3.68 ± 0.29	2761 ± 31	0.024	0.003	-	-	668 ± 304	
ESFa-2C.2	4.24 ± 0.27	2761 ± 31	0.049	0.003	-	-		
ESFa-2C.3	4.26 ± 0.81	2761 ± 31	0.074	0.006	-	-		
ESFa-4C.2	2.64 ± 0.19	2742 ± 18	0.080	0.005	-	-	1710 ± 3	
ESFa-5C.1	4.96 ± 0.19	2754 ± 32	0.063	0.003	-	-	722	
ESFa-6C.1.1	6.68 ± 0.33	2730 ± 21	0.089	0.005	-	-	700 ± 84	
ESFa-6C.1.2	6.72 ± 0.19	2730 ± 21	0.086	0.004	-	-		
ESFa-6C.2.1	7.00 ± 0.35	2730 ± 21	0.081	0.004	-	-		
ESFa-6C.2.2	7.00 ± 0.35	2730 ± 21	0.071	0.004	-	-		
ESFa-6C.2.3	7.02 ± 0.22	2730 ± 21	0.096	0.006	-	-		
ESFa-7C.1	7.18 ± 0.31	2773 ± 57	0.106	0.006	-	-	915 ± 137	
ESFa-7C.2	5.78 ± 0.36	2773 ± 57	0.088	0.010	-	-		
ESFa-7C.3	5.72 ± 0.19	2773 ± 57	0.109	0.006	-	-		
ESFa-7C.4	5.78 ± 0.36	2773 ± 57	0.108	0.007	-	-		
ESFa-7C.5	7.82 ± 0.22	2773 ± 57	0.107	0.013	-	-		
ESFa-9C.1	5.00 ± 0.21	2762 ± 12	0.064	0.003	0.082	0.004	585 ± 178	0.21 ± 0.04
ESFa-9C.2	4.56 ± 0.55	2762 ± 12	0.026	0.002	0.082	0.002		
ESFa-9C.3	4.56 ± 0.55	2762 ± 12	0.052	0.002	0.081	0.002		
ESFa-9C.4	3.72 ± 0.16	2762 ± 12	0.043	0.003	0.093	0.002		
ESFa-10C.1	5.22 ± 0.26	2731 ± 13	0.078	0.006	-	-	931 ± 97	
ESFa-10C.2	5.22 ± 0.26	2731 ± 13	0.083	0.007	-	-		
ESFa-10C.3	5.40 ± 0.21	2731 ± 13	0.098	0.007	-	-		

Sample	Thickness · 10^{-3} cm	δ_L g · l^{-1}	A_{1430}	*sd*	A_{3525}	*sd*	[CO_2] ppm	H_2O wt. %
ESFa-10C.3	5.40 ± 0.21	2731 ± 13	0.098	0.007	-	-		
ESFa-1B.1	4.40 ± 0.17	2731 ± 13	0.034	0.003	0.099	0.009	707 ± 267	0.24 ± 0.04
ESFa-1B.2	4.92 ± 0.16	2731 ± 13	0.060	0.003	0.124	0.006		
ESFa-1B.3	4.92 ± 0.16	2731 ± 13	0.085	0.004	0.086	0.006		
CO_2+Ne-bearing glass								
ESFa-1B.1	5.00 ± 0.25	2678 ± 46	0.105	0.010			1328 ± 158	
ESFa-1B.2	4.92 ± 0.27	2678 ± 46	0.122	0.006				
ESFa-2B.1	3.52 ± 0.19	2739 ± 75	0.079	0.004			1023 ± 259	
ESFa-2B.2	3.52 ± 0.19	2739 ± 75	0.064	0.006				
ESFa-2B.3	4.08 ± 0.30	2739 ± 75	0.055	0.004				
ESFa-3B.1	8.22 ± 0.11	2691 ± 7	0.099	0.003			721 ± 188	
ESFa-3B.2	8.22 ± 0.11	2691 ± 7	0.108	0.001				
ESFa-3B.3	8.22 ± 0.11	2691 ± 7	0.128	0.002				
ESFa-3B.4	7.32 ± 0.19	2691 ± 7	0.053	0.009				
ESFa-3B.5	5.68 ± 0.28	2691 ± 7	0.082	0.003				
ESFa-5B.1	2.58 ± 0.25	2755 ± 4	0.081	0.004			1705 ± 101	
ESFa-5B.2	2.66 ± 0.22	2755 ± 4	0.077	0.004				
ESFa-6B.1	4.16 ± 0.38	2758 ± 3	0.052	0.002	0.120	0.000	880 ± 240	0.30 ± 0.02
ESFa-6B.2	4.16 ± 0.38	2758 ± 3	0.077	0.001	0.107	0.001		
ESFa-7B.1	3.42 ± 0.22	2728 ± 8	0.090	0.002			1546 ± 66	
ESFa-7B.2	3.40 ± 0.43	2728 ± 8	0.095	0.003				
ESFa-10B.1	3.90 ± 0.22	2707 ± 5	0.087	0.004			1197 ± 119	
ESFa-10B.2	4.18 ± 0.18	2707 ± 5	0.081	0.003				
ESFa-2A.1	6.42 ± 0.20	2715 ± 20	0.120	0.004			1023 ± 63	
ESFa-2A.6	3.28 ± 0.13	2715 ± 20	0.056	0.002				
ESFa-5A.1	3.38 ± 0.84	2770 ± 36	0.064	0.003			1043 ± 47	

Sample	Thickness · 10^{-3} cm	δ_L g · l^{-1}	A_{1430}	*sd*	A_{3525}	*sd*	[CO_2] ppm	H_2O wt. %
ESFa-5A.2	3.40 ± 0.71	2770 ± 36	0.060	0.005				
EN-E3.1	4.76 ± 0.17	2770 ± 6	0.213	0.001	0.4330	0.0019	2385 ± 162	0.91 ± 0.06
EN-E3.2	4.76 ± 0.17	2770 ± 6	0.187	0.003	0.3600	0.0007		
EN-E3.3	4.76 ± 0.17	2770 ± 6	0.189	0.003	0.3932	0.0016		
EN-E3.4	4.76 ± 0.17	2770 ± 6	0.205	0.004	0.3864	0.0009		
EN-E3.5	4.76 ± 0.17	2770 ± 6	0.217	0.004	0.4038	0.0013		

Table S-7 Measured neon isotopic ratios (corrected for blanks) of the Ne-standard (for the Helix-SDT mass spectrometer). This set was analysed over sixteen months, the averages for the two isotopic ratios are represented with the associated 1sigma uncertainties. To correct for mass discrimination, averages of isotopic ratios and sensitivity measured on standards during the same period as for vesicles (Table S-8) were taken. The uncertainty of the average represents the standard deviation of the reported set standards.

	Sensitivity $^{22}Ne \cdot 10^{-15}$ (cm^3STP / cps)	$^{20}Ne/^{22}Ne$	$^{21}Ne/^{22}Ne$
STD_1	3.65	10.04 ± 0.02	0.0291 ± 0.0003
STD_2	3.69	10.30 ± 0.04	0.0289 ± 0.0002
STD_3	3.70	10.23 ± 0.03	0.0292 ± 0.0003
STD_4	3.67	10.20 ± 0.02	0.0290 ± 0.0001
STD_5	2.43	10.22 ± 0.03	0.0291 ± 0.0003
STD_6	3.78	10.34 ± 0.03	0.0287 ± 0.0002
STD_7	3.69	10.31 ± 0.03	0.0292 ± 0.0002
STD_8	3.70	10.23 ± 0.02	0.0288 ± 0.0002
STD_9	3.72	10.32 ± 0.04	0.0285 ± 0.0002
STD_10	3.68	10.27 ± 0.03	0.0294 ± 0.0002
STD_11	3.67	10.26 ± 0.03	0.0288 ± 0.0002
STD_12	3.61	10.20 ± 0.03	0.0290 ± 0.0003
STD_13	3.64	10.24 ± 0.02	0.0290 ± 0.0003
STD_14	3.73	10.27 ± 0.03	0.0283 ± 0.0003
STD_15	3.76	10.22 ± 0.03	0.0288 ± 0.0003
STD_16	3.73	10.18 ± 0.02	0.0286 ± 0.0002
STD_17	3.65	10.28 ± 0.03	0.0288 ± 0.0003
mean		**10.24 ± 0.07**	**0.0289 ± 0.0003**
STD_18	3.66	10.13 ± 0.03	0.0290 ± 0.0003
STD_19	3.64	10.02 ± 0.04	0.0287 ± 0.0002
STD_20	3.69	10.27 ± 0.03	0.0288 ± 0.0003
STD_21	3.74	10.38 ± 0.03	0.0288 ± 0.0003
STD_22	3.69	10.20 ± 0.03	0.0288 ± 0.0003
STD_23	3.68	10.29 ± 0.03	0.0288 ± 0.0003
STD_24	3.67	10.32 ± 0.04	0.0293 ± 0.0004
STD_25	3.68	10.32 ± 0.04	0.0284 ± 0.0003
STD_26	3.64	9.92 ± 0.03	0.0286 ± 0.0003
STD_27	3.65	10.03 ± 0.04	0.0286 ± 0.0002
STD_28	3.66	10.07 ± 0.04	0.0289 ± 0.0004
STD_29	3.66	10.15 ± 0.03	0.0286 ± 0.0002
STD_30	3.66	10.21 ± 0.02	0.0289 ± 0.0002
STD_31	3.71	10.09 ± 0.04	0.0293 ± 0.0003
STD_32	3.70	10.24 ± 0.04	0.0291 ± 0.0003
STD_33	3.72	10.19 ± 0.02	0.0292 ± 0.0004
mean		**10.18 ± 0.13**	**0.0289 ± 0.0003**

Table S-8 Measured ^{22}Ne abundances and Ne isotopic compositions obtained with the HELIX-SFT mass spectrometer of the vesicles for the experimental samples *ESFa-3B-204min*, *ESFa-5B-10min* and *ESFa-6B-10min*. Errors are 1 sigma uncertainties. Pb_{Tot} is the partial pressure resulting from vesicle gas expansion to the purification line when piercing. *Air* composition from (Ozima and Podosek, 2002). **The gas extracted in these vesicles corresponds to three vesicles pierced at the same time.

Sample	$Pb_{Tot} \cdot 10^{-7}$ bar	$^{22}Ne \cdot 10^{-12}$ cm^3 STP	$^{20}Ne/^{22}Ne$	$^{21}Ne/^{22}Ne$
ESFa-3B vesicles (240 min)				
V1	40	5.00 ± 0.10	9.97 ± 0.06	0.0288 ± 0.0006
V2**	79	6.36 ± 0.12	10.28 ± 0.05	0.0303 ± 0.0006
V3	26	3.33 ± 0.06	9.97 ± 0.09	0.0303 ± 0.0007
V4	22	4.00 ± 0.08	9.8 ± 0.06	0.0285 ± 0.0007
V5	165	18.25 ± 0.35	10.05 ± 0.05	0.0296 ± 0.0005
V6	14	2.51 ± 0.05	9.75 ± 0.08	0.0286 ± 0.0007
V7	11	1.93 ± 0.04	9.85 ± 0.12	0.0282 ± 0.0007
V1 ALA	19	2.08 ± 0.04	9.82 ± 0.08	0.0307 ± 0.0007
V2 ALA	15	2.51 ± 0.05	10.50 ± 0.13	0.0303 ± 0.0005
V3 ALA	350	3.84 ± 0.07	10.26 ± 0.10	0.0298 ± 0.0004
V4 ALA	9	1.73 ± 0.03	9.84 ± 0.08	0.0294 ± 0.0007
V5 ALA	11	1.67 ± 0.02	9.88 ± 0.10	0.0304 ± 0.0009
V6 ALA	9	1.20 ± 0.02	10.08 ± 0.11	0.0282 ± 0.0010
V7 ALA	6	0.98 ± 0.02	10.06 ± 0.09	0.0291 ± 0.0007
V8 ALA	13	2.04 ± 0.04	10.03 ± 0.10	0.0292 ± 0.0008
V9 ALA**	36	4.54 ± 0.09	9.73 ± 0.08	0.0292 ± 0.0005
V10 ALA	35	5.89 ± 0.11	9.76 ± 0.07	0.0288 ± 0.0004
V11 ALA	21	2.59 ± 0.05	9.77 ± 0.09	0.0287 ± 0.0007
ESFa-5B vesicles (10 min)				
V1	173	23.25 ± 0.26	9.97 ± 0.02	0.0289 ± 0.0002
V2	19	2.95 ± 0.03	10.03 ± 0.04	0.0289 ± 0.0004
V3	28	3.89 ± 0.04	9.96 ± 0.04	0.0290 ± 0.0005
V4	18	2.62 ± 0.03	10.24 ± 0.05	0.0302 ± 0.0005
V5	19	2.34 ± 0.03	10.02 ± 0.05	0.0284 ± 0.0005
V6	28	3.57 ± 0.04	9.80 ± 0.03	0.0284 ± 0.0004
V7	178	24.24 ± 0.27	9.81 ± 0.02	0.0293 ± 0.0001
V10	20	2.99 ± 0.03	9.62 ± 0.04	0.0283 ± 0.0003
V11	31	4.60 ± 0.05	9.44 ± 0.04	0.0296 ± 0.0002
V12	23	3.62 ± 0.04	9.73 ± 0.05	0.0300 ± 0.0005
ESFa-6B vesicles (10 min)				
V1	9	1.45 ± 0.01	9.40 ± 0.08	0.0264 ± 0.0009
V2	49	5.01 ± 0.05	9.56 ± 0.03	0.0297 ± 0.0005
V3	9	1.49 ± 0.01	9.58 ± 0.07	0.0289 ± 0.0008
Air			9.8	0.0290
MFF_{Ne}			10.28	0.0297

Table S-9 Vesicle size distribution parameters of the experimental samples analysed by microtomography. The image treatment was done by using *ImageJ*. *Nb* represents the number of counted bubbles in one slice of the image stack obtained by the tomography; *Area* is the analysed surface of the glass; Bubble density corresponds to the number of vesicles by surface area; D_{max} and D_{mean} correspond to the maximum and mean diameter of the vesicles of the scanned slice; *Ln(n)* is the density of the population of vesicles obtained by the linear regression of *Ln(n)* vs D_{max}; *a* is the slope of the trend line; R^2 is the correlation coefficient of the trend line; $D_{mean.th}$ is the theoretical mean diameter obtained by the inverse of the slope (-1/a); *Ves.* is the obtained vesicularity by VGSudioMax.

Sample	Nb	Area (mm^2)	Bubbles density (mm^{-2})	D_{max} (µm)	D_{mean} (µm)	Ln(n) (mm^{-4})	a (mm^{-1})	R^2	$D_{mean.th.}$ (-1/a) (µm)	Ves (%)
CO_2-bearing glass										
ESFa-4	376	9.0	41.9	99.9	19.8	12.5 ± 0.3	-66.9 ± 5.8	0.9	15.0	0.9
ESFa-8	145	4.8	30.1	118.8	19.5	12.0 ± 0.4	-63.7 ± 7.8	0.9	15.7	0.5
ESFa-10	196	12.1	16.2	108.3	21.3	11.3 ± 0.4	-62.9 ± 7.7	0.9	15.9	0.6
ESFa-10E	497	12.8	38.7	102.8	20.1	12.3 ± 0.3	-63.6 ± 6.8	0.9	15.7	0.7
ESFa-2D	64	2.9	21.8	179.7	33.1	10.3 ± 0.6	-36.4 ± 7.2	0.7	27.4	0.8
ESFa-3D	555	11.4	48.6	140.0	23.1	12.3 ± 0.2	-56.1 ± 3.7	1.0	17.8	0.9
ESFa-8D	209	13.4	15.6	229.7	24.9	10.7 ± 0.4	-46.0 ± 3.8	0.9	21.7	1.4
ESFa-1C	583	10.4	56.1	322.3	28.0	10.9 ± 0.5	-30.2 ± 3.4	0.9	33.1	4.2
ESFa-2C	400	11.8	33.8	140.4	22.0	12.4 ± 0.5	-63.2 ± 6.1	0.9	15.8	0.2
ESFa-4C	332	5.2	64.5	144.0	18.2	13.4 ± 0.5	-80.6 ± 8.0	0.9	12.4	2.0
ESFa-5C	490	12.0	40.8	159.4	24.4	11.8 ± 0.4	-49.5 ± 5.3	0.9	20.2	1.6
ESFa-6C	451	12.9	35.0	163.5	15.5	12.4 ± 0.4	-73.7 ± 5.7	0.9	13.6	0.5
ESFa-7C	223	9.8	22.8	158.1	23.3	11.3 ± 0.5	-52.3 ± 6.9	0.9	19.1	1.1
ESFa-9C	257	4.9	52.0	168.5	26.4	11.9 ± 0.5	-45.7 ± 5.9	0.9	21.9	3.1
ESFa-10C	524	16.1	32.6	159.2	24.9	11.8 ± 0.3	-52.5 ± 4.0	0.9	19.0	2.2
ESFa-1B	732	12.8	57.3	170.1	20.3	12.9 ± 0.5	-67.4 ± 5.9	0.9	14.8	2.0
CO_2+Ne-bearing glass										
ESFa-1B	384	9.5	40.5	119.8	18.0	12.6 ± 0.3	-70.1 ± 4.9	1.0	14.3	1.5
ESFa-2B	1111	13.9	80.2	191.1	16.6	13.5 ± 0.4	-77.1 ± 5.0	1.0	13.0	1.2

Sample	Nb	Area (mm^2)	Bubbles density (mm^{-2})	D_{max} (µm)	D_{mean} (µm)	Ln(n) (mm^{-4})	a (mm^{-1})	R^2	$D_{mean.th.}$ (-1/a) (µm)	Ves (%)
ESFa-3B	953	10.6	89.7	161.8	18.5	12.9 ± .5	-60.3 ± 7.0	0.9	16.6	1.7
ESFa-5B	133	11.3	11.8	196.6	37.9	9.5 ± 0.6	-32.0 ± 6.2	0.7	31.3	0.9
ESFa-6B	39	5.6	6.9	90.6	29.5	10.1 ± 1.4	-51.7 ± 11.6	0.7	19.4	0.4
ESFa-7B	494	13.3	37.1	166.2	22.6	11.6 ± 0.4	-47.8 ± 5.5	0.9	20.9	4.0
ESFa-10B	157	4.7	33.3	91.4	19.8	12.1 ± 0.3	-63.4 ± 7.2	0.9	15.8	0.8
ESFa-2A	702	10.3	68.0	160.9	17.3	12.5 ± 0.5	-56.7 ± 5.9	0.9	17.6	0.5
ESFa-5A	308	8.1	37.9	273.7	30.3	10.5 ± 0.7	-31.1 ± 5.2	0.8	32.1	2.5
EN-E3	-	-	-	-	-	-	-	-	-	-

Table S-10 CO_2 diffusion in the melt (D_{CO2}), bubble displacement (B_d) and bubble growth (G_r) at the time at which the experiments were quenched.

Sample	$time_{exp}$ min	D_{CO2} (cm)	B_d (cm)	G_r (cm)
CO_2-bearing glass				
ESFa-4	30	1.3E-02	2.5E-03	2.5E-05
ESFa-8	240	3.6E-02	3.1E-02	2.1E-04
ESFa-10	240	3.6E-02	3.7E-02	2.1E-04
ESFa-10E	1140	7.9E-02	2.9E-01	1.0E-03
ESFa-2D	1140	7.9E-02	7.1E-01	1.7E-03
ESFa-3D	130	2.7E-02	1.5E-02	1.3E-04
ESFa-8D	360	4.4E-02	4.8E-02	4.3E-04
ESFa-1C	10	7.4E-03	1.7E-03	1.8E-05
ESFa-2C	10	7.4E-03	1.0E-03	8.8E-06
ESFa-4C	60	1.8E-02	4.2E-03	4.1E-05
ESFa-5C	60	1.8E-02	7.7E-03	6.7E-05
ESFa-6C	240	3.6E-02	1.2E-02	1.8E-04
ESFa-7C	240	3.6E-02	2.8E-02	2.5E-04
ESFa-9C	10	7.4E-03	2.9E-03	1.2E-05
ESFa-10C	240	3.6E-02	3.2E-02	2.5E-04
ESFa-1B	10	7.4E-03	1.8E-03	8.2E-06
CO_2+Ne-bearing glass				
ESFa-1B	240	3.7E-02	1.6E-02	1.9E-04
ESFa-2B	240	3.7E-02	1.4E-02	1.7E-04
ESFa-3B	240	3.7E-02	1.7E-02	2.2E-04
ESFa-5B	10	7.5E-03	3.1E-03	1.7E-05
ESFa-6B	10	7.5E-03	4.3E-03	1.1E-05
ESFa-7B	240	3.6E-02	2.6E-02	2.8E-04
ESFa-10B	240	3.6E-02	2.0E-02	2.1E-04
ESFa-2A	240	3.6E-02	1.5E-02	2.4E-04
ESFa-5A	10	7.4E-03	2.0E-03	1.8E-05
EN-E3	1800	9.9E-02	-	-

Supplementary Figures

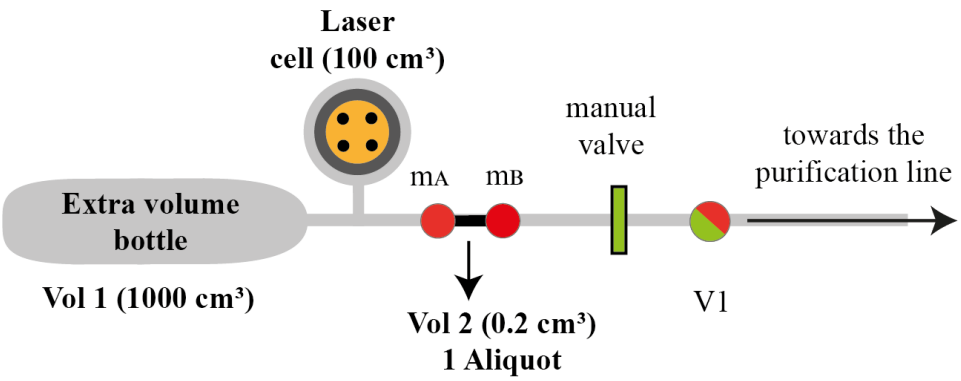

Figure S-1 Extraction and under-vacuum expansion volume attached to the purification line of the Noblesse mass spectrometer type (not at scale). The automatic valve, V1, is controlled by LabVIEW ©. The red circles show the manual valves for controlling Vol 2; the green rectangle valve isolates the expansion volume line from the purification line and V1, representing the automatic valve leading to the purification line. The extra volume bottle represents Vol 1 (1000 cm^3). The laser cell holds the chunk of glass to be analysed and consists of a volume of 100 cm^3 (Vol 3).

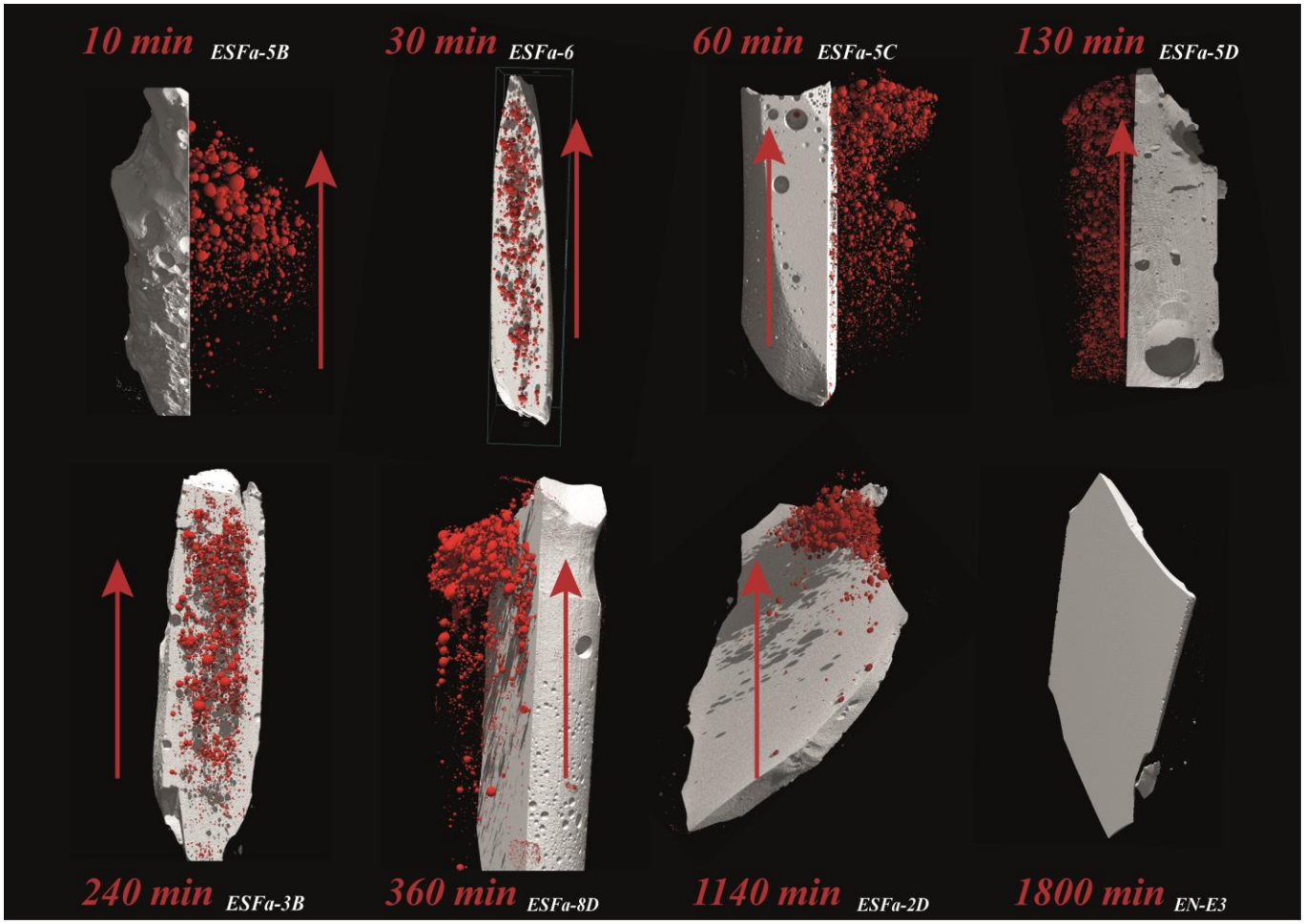

Figure S-2 3D Representative images for every experimental time. The experiment time increases from 10 to 1800 minutes, from top to bottom of the image. The accumulation of vesicles at one of the limits of the sample is evident when the experimental time increases until there are no more vesicles (at 1800 min of the experiment). The length of samples ranges from 1 to 1.2 cm. The red line marks the direction of bubble flow towards the top of the capsule.

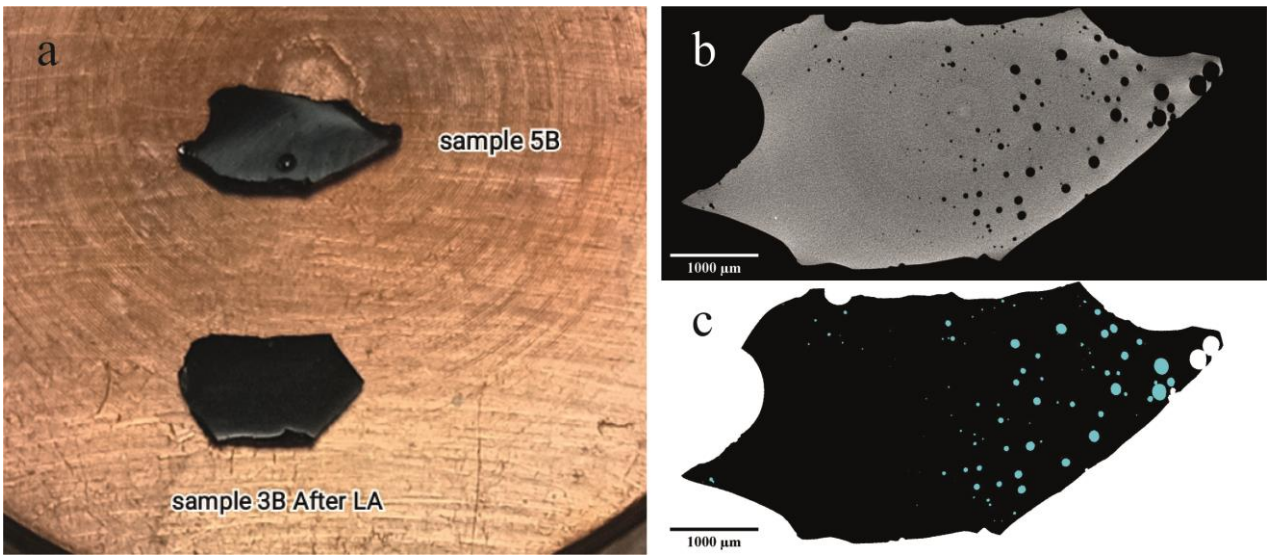

Figure S-3 (a) *ESFa-3B-240min* (approximately 5 mm in length) and *ESFa-5B-10min* samples (approximately 7 mm in length) placed inside the laser cell. The images on the right display the *ESFa-5B-10min* sample, with the image obtained through tomography **(b)** and further processed using *ImageJ* **(c)** to determine the vesicle size distribution.

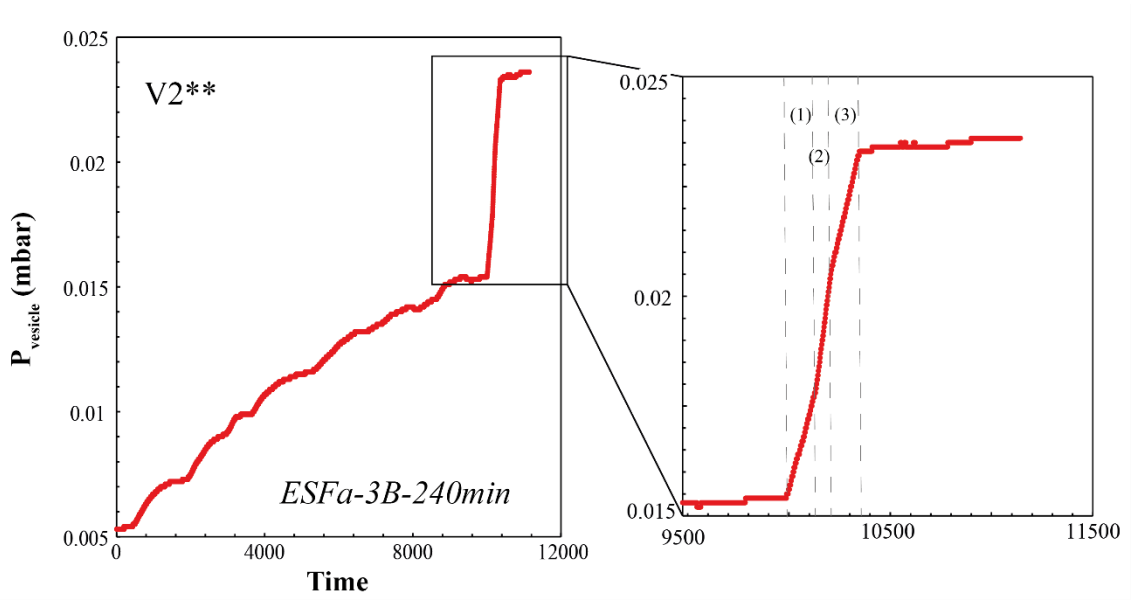

Figure S-4 Partial pressure in mbar, as recorded by the manometer, during laser ablation of three vesicles from sample *ESFa-3B-240min*. The blow-up on the right reveals three changes in the slope of the pressure curve. Dashed lines mark the representative pressure for each pierced vesicle, labelled (1), (2), and (3) in the right-hand plot. The time is not represented in specific units but is instead recorded by the software.

Supplementary Information References

Behrens, H., Zhang, Y. (2001) Ar diffusion in hydrous silicic melts: implications for volatile diffusion mechanisms and fractionation. *Earth Planetary Science Letters* 192, 363–376. https://doi.org/10.1016/S0012-821X(01)00458-7

Bottinga, Y., Richet, P., (1981) High pressure and temperature equation of state and calculation of the thermodynamic properties of gaseous carbon dioxide. *American Journal of Sc*ience 281, 615–660. https://doi.org/10.2475/ajs.281.5.615

Di Carlo, I., Pichavant, M., Rotolo, S.G., Scaillet, B. (2006) Experimental crystallization of a high-K arc basalt: the golden pumice, Stromboli volcano (Italy). *Journal of Petrol*ogy 47, 1317–1343. https://doi.org/10.1093/petrology/egl011

Giordano, D., Russell, J.K., Dingwell, D.B. (2008) Viscosity of magmatic liquids: a model. *Earth Planetary Science Lett*ers 271, 123–134. https://doi.org/10.1016/j.epsl.2008.03.038

Jambon, A., Weber, H., Braun, O. (1986) Solubility of He, Ne, Ar, Kr and Xe in a basalt melt in the range 1250–1600 C. Geochemical implications. *Geochimica Cosmochimica Acta* 50, 401–408. https://doi.org/10.1016/0016-7037(86)90193-6

Jiménez-Mejías, M., Andújar, J., Scaillet, B., Casillas, R. (2021) Experimental determination of H_2O and CO_2 solubilities of mafic alkaline magmas from Canary Islands. *Comptes Rendus Géoscience* 353, 289–314. https://10.5802/crgeos.84

Lange, R.A. (1994) Volatiles in Magmas. In: Carroll, M.R., Holloway, J.R. (Eds.). *De Gruyter, pp*. 331–370. https://doi.org/10.1515/9781501509674-015

Nowak, M., Schreen, D., Spickenbom, K. (2004) Argon and CO_2 on the race track in silicate melts: a tool for the development of a CO2 speciation and diffusion model. *Geochimica Cosmochimica Acta* 68, 5127–5138. https://doi.org/10.1016/j.gca.2004.06.002

Ozima, M., Podosek, F.A. (2002) Noble gas geochemistry. *Cambridge University Press*. https://doi.org/10.1017/CBO9780511545986

Sarda, P., Graham, D. (1990) Mid-ocean ridge popping rocks: implications for degassing at ridge crests. *Earth and Planetary Science Letters* 97, 268–289. https://doi.org/10.1016/0012-821X(90)90047-2

Stolper E. (1982) The speciation of water in silicate melts. *Geochimica Cosmochimica Acta* 46:2609–2620. https://doi.org/10.1016/0016-7037(82)90381-7.

Stout, V.L., Gibbons, M.D. (1955) Gettering of gas by titanium. *Journal of Applied Phys*ics 26, 1488–1492. https://doi.org/10.1063/1.1721936

Warren, P.H. (1995) Extrapolated partial molar densities of SO_3, P_2O_5, and other oxides in silicate melts. *American Mineral*ogist 80, 1085–1088. https://doi.org/10.2138/am-1995-9-1029

Watson, E.B., Sneeringer, M.A., Ross, A. (1982) Diffusion of dissolved carbonate in magmas: experimental results and applications. *Earth and Planetary Science Lett*ers 61, 346–358. https://doi.org/10.1016/0012-821X(82)90065-6

Zhang, Y., Xu, Z. (1995) Atomic radii of noble gas elements in condensed phases. *American Mineralogist* 80, 670–675. https://doi.org/10.2138/am-1995-7-803

Zhang, Y., Xu, Z., Zhu, M., Wang, H. (2007) Silicate melt properties and volcanic eruptions. *Reviews in Geophysics* 45. https://doi.org/10.1029/2006RG000216

« Digital modelling platform» https://calcul-isto.cnrs-orleans.fr/apps/propagator/